Optimisation of the Hydraulic Variable Inertia Flywheel for Specific Energy

Arne Rettig[1]*, Lisanne Reese[2], Clemens Jauch[3]

[1] Wind Energy Technology Institute (WETI), Flensburg University of Applied Sciences, 24943 Flensburg, Germany, +49 461 48 161 441, arne.rettig@hs-flensburg.de
[2] +49 461 48161 107, lisanne.reese@hs-flensburg.de
[3] +49 461 48161 108, clemens.jauch@hs-flensburg.de

Abstract: *The ongoing transition towards inverter-based generation is significantly reducing conventional rotational inertia in power systems, leading to increased rates of change of frequency. To address this challenge, the Hydraulic Variable Inertia Flywheel (HVI-FW) represents a novel alternative for distributed and inherent inertia provision. This paper presents a design tool developed to optimize the geometric parameters of the novel flywheel, with respect to specific energy. A parameter study is conducted by varying key geometric dimensions, such as radius and height. The results demonstrate that the HVI-FW can achieve significantly higher specific energy than conventional flywheels, particularly for small radii, making it well suited for coupling with small, synchronously rotating electrical machines. The findings highlight the potential of the HVI-FW as an effective solution for providing distributed inertia in future low-inertia power systems.*

Keywords: Flywheel, Inertia, Power System Inertia, Energy Storage, Electrical Machines

1 Introduction

The control of the European electricity grid currently relies on conventional inertia provided by rotational masses connected to the grid via synchronous generators [1]. The kinetic energy (E_{kin}) stored within these rotating generator units responds inherently, opposing power imbalances (ΔP) [2]. Power imbalances lead to a change in the frequency (f) of the electricity grid. The instantaneous Rate of Change of Frequency $(RoCoF)$ can be derived from equation (1), where S_{sys} and H_{sys} are the apparent power and the inertia constant of the power grid [3, 4].

$$RoCoF = \frac{\Delta P \cdot f}{2 \cdot \underbrace{S_{sys} \cdot H_{sys}}_{E_{kin}}} \tag{1}$$

It becomes apparent that the kinetic energy stored in the power grid (E_{kin}) is crucial to keep the $RoCoF$ within manageable limits [3]. The transition towards 100 % renewable energy is rapidly reducing conventional inertia, as synchronously rotating generation units are replaced by inverter-based renewables [2]. This can be supported by frequency measurements from Thiesen et al. 2021 [5] that show an increase in $RoCoF$ in the continental European electricity grid from 2016 to 2022, see Figure 1. Furthermore, the figure shows that the $RoCoF$ tends to be lower in the winter periods and higher in the summer periods. This is most likely due to increased generation from inverter-based plants during the summer periods and the associated substitution of conventional rotating generation plants.

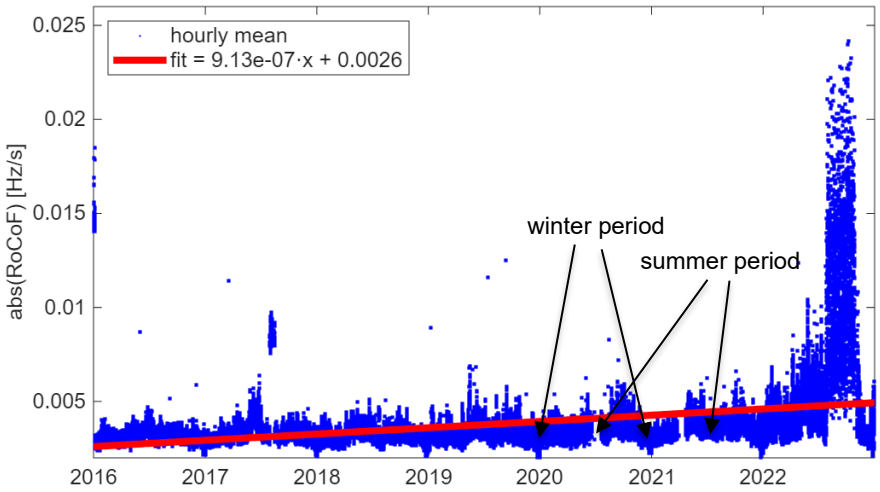

Figure 1: Hourly mean of the absolute RoCoF in the continental European electricity grid from 2016 to 2022. The data points (blue) are fitted with a linear function (red) over the entire data series.

To maintain a stable frequency control in a future European electricity grid, additional synthetic inertia together with alternative spinning reserves is required [2]. The Hydraulic Variable Inertia Flywheel (HVI-FW) [6] represents such an alternative spinning reserve [6, 7]. It is a synchronously rotating flywheel that can store energy in the change of its rotational speed, in the change of its moment of inertia and in the compression of gas [6]. Thus, the HVI-FW is offering a greater specific energy (Wh/kg) compared to conventional flywheels (CFWs), making it a valuable addition for providing inertia to the electricity grid. This novel flywheel therefore addresses a critical need in a future continental European electricity grid by offering distributed, fast-responding, inherent inertia. In section 3 the specific energy of the HVI-FW is discussed in more detail. In order to show which geometric configurations of the HVI-FW are best suited for this task, this paper introduces a design tool developed for this purpose.

2 Design Tool

The design tool operates according to the flow diagram shown in Figure 2. The nominal operational speed of the HVI-FW is set to 50 Hz, since this is the nominal rotational speed of directly grid connected synchronous machines, which the HVI-FW shall be connected to. The lowest and highest permissible power system frequencies are 47.5 Hz and 51.5 Hz [8]. Therefore these frequencies serve as limit values for the design tool. In the starting script multiple sets of geometric and initial operating parameters for a rotational speed of 50 Hz are fed into the design tool, see section 2.1. Subsequently, the fluid displacement inside the HVI-FW is determined for each parameter set for an increase in speed to 51.5 Hz and also for a reduction in speed to 47.5 Hz (see section 2.2). The fluid displacement and the resulting gas and centrifugal pressures at 51.5 Hz form the basis for the strength calculation, as they are highest at this speed, see section 2.3. The resulting fluid levels in the hollow and central cylinders at 47.5 Hz are used to calculate the mass and the moment of inertia of the HVI-FW, see section 2.4. Now that the required material thicknesses and process parameters at the relevant operating points are known, the specific energy of the HVI-FW for a discharge cycle from 50 to 47.5 Hz can finally be determined. The specific energy is of special interest, because the HVI-FW can achieve advantages over conventional flywheels in this respect.

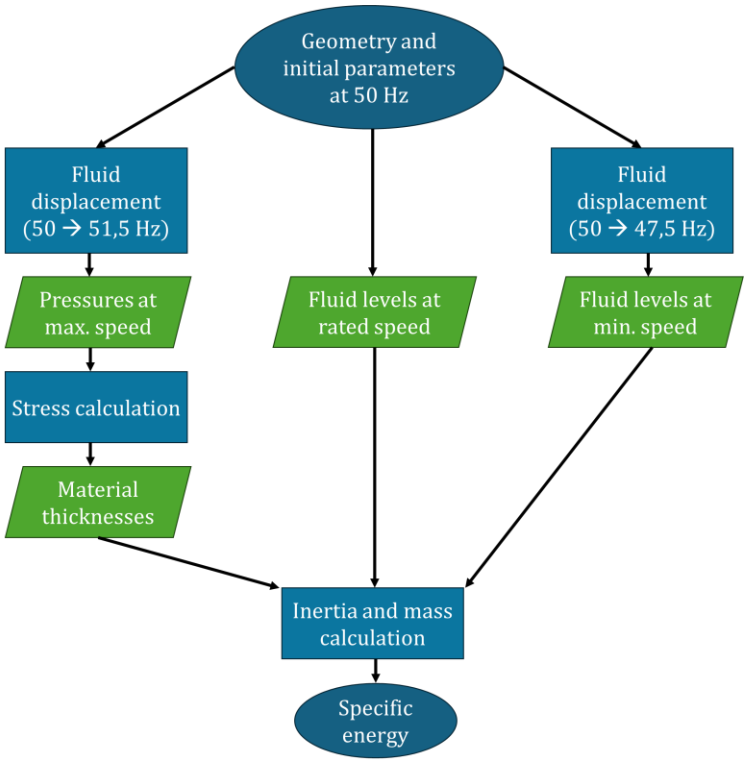

Figure 2: Flow diagram for determining the specific energy for each geometric configuration of the HVI-FW

2.1 Geometry and Initial Operating Parameters

Before the geometrical optimisation can be started, the input parameters shown in Table 1 have to be defined in the starting script. More detailed explanations of these parameters are given in Jauch et al. 2024 [6]. Of particular importance are the vectors that define the ranges of cylinder radii and cylinder heights (R_i, r_i, H_{total}). These ranges define the possible dimensions of the HVI-FW within which the optimum in specific energy is to be found. These must be defined by the user.

Table 1: Geometry and initial operating parameters that serve as input for the design tool

variable	value	explanation
n_0	50 [Hz]	Rated speed of the HVI-FW
n_{up}	51.5 [Hz]	Upper speed limit
n_{low}	47.5 [Hz]	Lower speed limit
p_{atm}	1 [bar]	Gas pressure in the central cylinder
SF	2	Safety factor
g	9.81 [m/s²]	Gravitational acceleration
n_{BH}	4	Number of radial bulkheads
SoC_{n_0}	62.50%	State of Charge at n_0, i.e. share of fluid inside the hollow cylinder
$\rho_{PETG}, \rho_{CFRP}, \rho_{fl}$	1250, 1800, 1000 [kg/m³]	Density of PETG, CFRP & fluid
$\sigma_{PETG}, \sigma_{CFRP}$	50, 2500 [MPa]	Yield strength of PETG & CFRP
E_{PETG}, E_{CFRP}	2.2, 160 [GPa]	Modulus of elasticity of PETG & CFRP
v_{PETG}, v_{CFRP}	0.4, 0.28	Poisson's ratio of PETG and CFRP
R_i	Variable vector	Range of hollow cylinder inner radii [m]
r_i	Variable vector	Range of central cylinder inner radii [m]
H_{total}	Variable vector	Range of central cylinder heights [m]

Another key element of the design tool are the assumptions about the geometry of the HVI-FW, presented in Figure 3. This figure serves as the basis for all subsequent calculations. When reading the following subsections, the reader can return to Figure 3 for graphical explanations of used variables and parameters. As shown in Figure 3, the HVI-FW consists of a 3D-printed liner (coloured in green) made from polyethylene terephthalate glycol (PETG). This liner defines the internal structure and thus the geometry of the central cylinder, the hollow cylinder and the fluid channels connecting the two cylinders. To ensure that the HVI-FW has the necessary strength to withstand the centrifugal forces and internal pressures acting on it, when rotating at up to 51.5 Hz the liner is wrapped with carbon fibre reinforced polymer (CFRP).

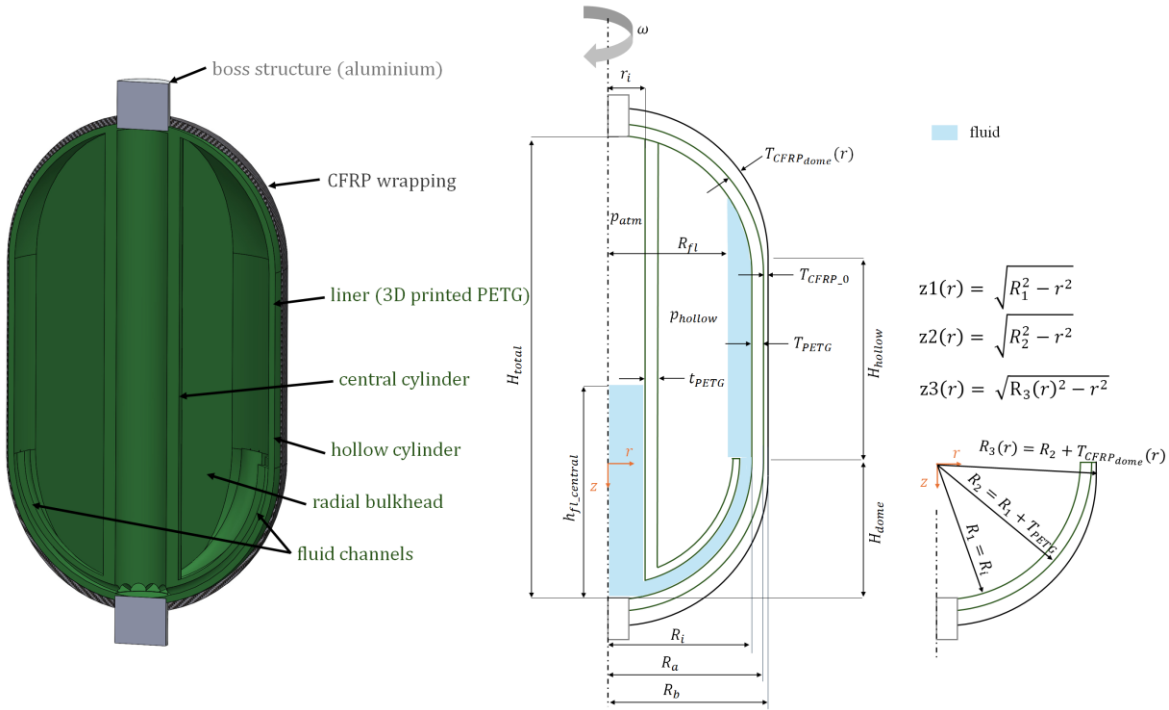

Figure 3: 3D sectional view and abstracted geometry of the HVI-FW considered in the design tool

Aluminum boss structures are provided at the ends of the HVI-FW, through which the flywheel can be pressurised with gas and supported with bearings (gas channels are not visible in the drawing).

It is assumed that the fluid channels are always filled with fluid. Further, when completely discharged, the central cylinder is filled completely and no fluid remains in the hollow cylinder. Therefore, the volume of the displaceable fluid (dV_{max}) can be calculated from equation (2), see Figure 3.

$$dV_{max} = \pi \cdot {r_i}^2 \cdot H_{total} \tag{2}$$

Where r_i is the inner radius and H_{total} is the inner height of the central cylinder, both defined by the user of the design tool (see Table 1).

The inner contour of the dome-shaped lids is approximated using the circle equation $z1(r)$, see equation (3) and Figure 3.

$$z1(r) = \sqrt{{R_i}^2 - r^2} \tag{3}$$

By determining $z1(r = 0)$, the height of the dome-shaped lids (H_{dome}) can be calculated. Knowing H_{dome} the height of the hollow cylinder H_{hollow} can be obtained with equation (4).

$$H_{hollow} = H_{total} - 2 \cdot H_{dome} \tag{4}$$

The fluid volume contained in the hollow cylinder ($V_{fl_{hollow}}$), when rotating at nominal speed (50 Hz), can be derived from the state of charge (SoC_{n_0}) defined in Table 1, applying equation (5).

$$V_{fl_{hollow}}(n_0) = dV_{max} \cdot \frac{SoC_{n_0}}{100\ \%} \tag{5}$$

The fluid volume in the central cylinder ($V_{fl_{central}}$), when rotating at n_0 can now also be determined, see equation (6).

$$V_{fl_{central}}(n_0) = dV_{max} - V_{fl_{hollow}}(n_0) \tag{6}$$

Using equation (3) the gas volume contained in the hollow cylinder can be calculated using the shell integration as described in equation (7) [9].

$$V_{gas_{hollow}}(n_0) = \pi \cdot H_{hollow} \cdot \left(R_i^2 - (r_i + t_{PETG})^2\right) + 2 \cdot 2\pi \cdot \left(\int_{(r_i+t_{PETG})}^{R_i} z1(r) \cdot r \cdot dr\right) - V_{fl_{hollow}}(n_0) \tag{7}$$

From the fluid volume in the central cylinder $V_{fl_{central}}(n_0)$, the fluid level $h_{fl_{central}}(n_0)$ can be calculated, see equation (8). It has to be noted that $h_{fl_{central}}(n_0)$ is an artificial value, as under rotation, the fluid surface is not a horizontal plane, but a paraboloid [6].

$$h_{fl_{central}}(n_0) = \frac{V_{fl_{central}}(n_0)}{\pi \cdot r_i^2} \tag{8}$$

The computation of the fluid level in the hollow cylinder (R_{fl} – see Figure 3) is required frequently in the fluid displacement calculation. Therefore, it is derived only once for a set of discrete values of $V_{fl_{hollow}}$, see Figure 4 . Subsequently, a third-order polynomial is fitted to this data in order to reduce the computational burden in later calculations. Thus, only the polynomial approximation (R_{fl_fit}) needs to be evaluated thereafter.

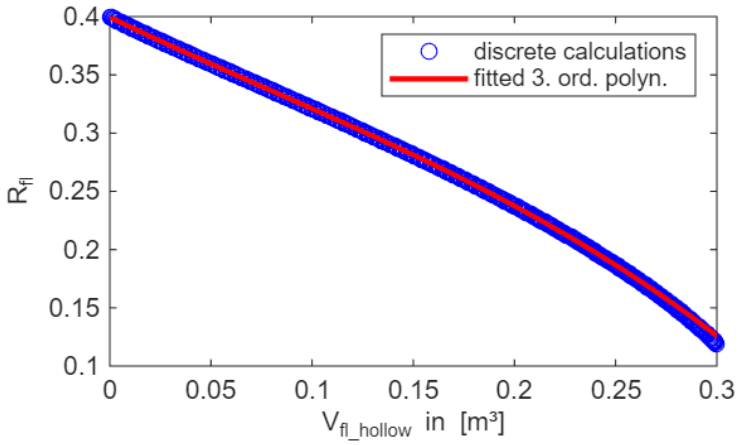

Figure 4: Fluid level in the hollow cylinder (R_{fl}) versus hollow cylinder fluid volume ($V_{fl_{hollow}}$).

2.2 Fluid Displacement

The fluid levels (R_{fl} and $h_{fl_{central}}$) evolve at rated speed (n_0), because a certain gas pressure is acting on the fluid in the hollow cylinder. This gas pressure (p_{hollow}) is crucial for the working principle of the HVI-FW and can be determined using equation (9). The pressure p_{hollow} is also shown in Figure 3.

$$\begin{aligned} &p_{hollow}(n_0) \\ &= \left(p_{atm} + \frac{\rho_{fl}}{2} \cdot \omega(n_0)^2 \cdot R_i^2 + \rho_{fl} \cdot g \cdot h_{fl_{central}}(n_0)\right) \\ &- \left(\frac{\rho_{fl}}{2} \cdot \omega(n_0)^2 \cdot \left(R_i^2 - R_{fl}(n_0)^2\right) + \rho_{fl} \cdot g \cdot (H_{hollow} + H_{dome})\right) \end{aligned} \tag{9}$$

The known fluid levels (R_{fl} and $h_{fl_{central}}$) at the rated speed (n_0) can be used to calculate the fluid levels that arise at speeds that are different from n_0. This is done by virtually displacing tiny amounts of fluid (dV) and thereby changing fluid levels (R_{fl} and $h_{fl_{central}}$) according to equations (10) and (11). This variation in fluid levels then leads to a pressure variation in the compressed gas in the hollow cylinder according to equation (12).

$$R_{fl}(n_{new}) = R_{fl\_fit}\left(V_{fl_{hollow}}(n_0) + dV\right) \tag{10}$$

$$h_{fl_{central}}(n_{new}) = \frac{V_{fl_{central}}(n_0) - dV)}{\pi \cdot r_i^2} \tag{11}$$

$$p_{hollow}(n_{new}) = P_{hollow}(n_0) \cdot \left(\frac{V_{gas_{hollow}}(n_0)}{V_{gas_{hollow}}(n_0) - dV}\right)^{1.4} \tag{12}$$

This procedure is repeated with increasing fluid displacement ($dV_{n+1} = dV_n + dV$) until the pressure error at the new speed n_{new}, which is described in equation (13), is less than 1 Pascal, or until the maximum permissible fluid volume dV_{max} is reached.

$$\begin{aligned} &error(new) \\ &= abs\left(p_{atm} + \frac{\rho_{fl}}{2} \cdot \omega(n_{new})^2 \cdot R_i^2 + \rho_{fl} \cdot g \cdot h_{fl_{central}}(n_{new})\right. \\ &\left. - p_{hollow}(n_{new}) - \frac{\rho_{fl}}{2} \cdot \omega(n_{new})^2 \cdot (R_i^2 - R_{fl}(n_{new})^2) - \rho_{fl} \cdot g \cdot (H_{hollow} + H_{dome})\right) \end{aligned} \tag{13}$$

2.3 Stress Calculation

Knowledge about the required wall thicknesses to withstand the internal pressure and centrifugal forces is necessary to evaluate different designs of the HVI-FW in regard of energy density, CO_2 emissions or the ratio of variable to stationary inertia. Therefore, the required wall thickness of the central cylinder, the hollow cylinder and the dome-shaped lids are determined subsequently.

2.3.1 Wall thickness PETG (t_{PETG}, T_{PETG})

The central cylinder is subject to the gas pressure in the hollow cylinder (p_{hollow}). Inside the central cylinder is always the negligible atmospheric pressure, (p_{atm}). Therefore, the wall thickness of the central cylinder (t_{PETG}) is designed to withstand buckling according the AD 2000 guidelines shown in equation (14) [10]. For p_{hollow} the gas pressure in the hollow cylinder, when accelerating the HVI-FW to 51.5 Hz is applied, see section 2.2.

$$\frac{E_{PETG}}{S_K} \cdot \frac{20}{1 - {v_{PETG}}^2} \cdot \left(\frac{t_{PETG} - c_1 - c_2}{2 \cdot (r_i + t_{PETG})}\right)^3 \geq p_{hollow} \tag{14}$$

E_{PETG} is the Modulus of elasticity and v_{PETG} is the Poisson's ratio, see Table 1. The parameters c_1 and c_2, specified by the AD 2000 guideline, are additional safety margins of 0.5 mm and 1 mm, respectively. They take into account fluctuations in material thickness and material wear. S_K is the safety factor to prevent buckling and equals three [10]. In the design tool, the wall thickness of the central cylinder (t_{PETG}) is increased in 1 mm increments until equation (14) is satisfied.

The wall thickness of the hollow cylinder made from PETG (T_{PETG}) is set to be half of the wall thickness of the central cylinder ($T_{PETG} = t_{PETG} / 2$). This is because the hollow cylinder wall made of PETG does not need to provide strength, and only provides gas tightness. Strength is ensured by the CFRP wrapping.

Knowing T_{PETG}, the outer contour of the dome-shaped lids made from PETG can be determined by the circle equation $z2(r)$, see equation (15). This contour forms the interface between the PETG liner and the CFRP wrapping.

$$z2(r) = \sqrt{(R_i + T_{PETG})^2 - r^2} \tag{15}$$

2.3.2 Wall thickness CFRP (T_{CFRP_0}, $T_{CFRP_{dome}}$)

The required wall thickness of the CFRP wrapping of the cylindrical section (T_{CFRP_0}) is determined by calculating the tangential and the axial stresses caused by the sum of the internal pressure components (P_i) and the centrifugal forces acting on the CFRP wrapping. The hollow cylinder wall made of PETG is assumed to be non-load-bearing.

The sum of the internal pressure components (P_i) acting on the CFRP at a rotational speed of 51.5 Hz is determined by equation (16), together with section 2.2.

$$P_i = p_{hollow}(n_{up}) + \frac{\rho_{fl}}{2} \cdot \omega(n_{up})^2 \cdot \left(R_i^2 - R_{fl}(n_{up})^2\right) + \frac{\rho_{PETG}}{2} \cdot \omega(n_{up})^2 \cdot \left({R_a}^2 - {R_i}^2\right) \tag{16}$$

The normal stresses in tangential (σ_t) and axial (σ_a) direction can be obtained from equations (17) and (18) respectively, according Grote & Feldhusen 2014 (Chapter C 6.3.5 and R 1.8) [11]. R_a denotes the inner radius of the CFRP wrapping ($R_a = R_i + T_{PETG}$) and R_b denotes the outer radius of the CFRP wrapping ($R_b = R_i + T_{PETG} + T_{CFRP\_0}$). Hence, $T_{CFRP\_0} = R_b - R_a$. The normal stresses are the greatest at the inside of the cylinder wall (at R_a), and are therefore calculated for this radius. The term $\omega(n_{up})$ represents the angular velocity at the upper speed limit.

$$\sigma_t(R_a) = \underbrace{\rho_{CFRP} \cdot \omega(n_{up})^2 \cdot {R_b}^2 \cdot \frac{(3 - 2 \cdot v_{CFRP})}{8 \cdot (1 - v_{CFRP})} \cdot \left(2 + \frac{{R_a}^2}{{R_b}^2} - \frac{(1 + 2 \cdot v_{CFRP}) \cdot {R_a}^2}{(3 - 2 \cdot v_{CFRP}) \cdot {R_b}^2}\right)}_{due\ to\ centrifugal\ forces} \underbrace{-p_{atm} + \frac{{R_b}^2 + {R_a}^2}{{R_b}^2 - {R_a}^2} \cdot (P_i - p_{atm})}_{due\ to\ internal\ pressure} \tag{17}$$

$$\sigma_a(R_a) = \underbrace{\rho_{CFRP} \cdot \omega(n_{up})^2 \cdot {R_b}^2 \cdot \frac{(2 \cdot v_{CFRP})}{8 \cdot (1 - v_{CFRP})} \cdot \left(1 - \frac{{R_a}^2}{{R_b}^2}\right)}_{due\ to\ centrifugal\ forces} + \underbrace{\frac{{R_a}^2 \cdot P_i - {R_b}^2 \cdot p_{atm}}{{R_b}^2 - {R_a}^2}}_{due\ to\ internal\ pressure} \quad (18)$$

The tensile strength of CFRP is anisotropic, due to the fibre orientation, see equation (19) [12]. The parameter A accounts for different fibre lengths and is set to 0.5 in the design tool. Accordingly, from equation ((19) a fibre angle φ is determined that enables the CFRP wrapping to withstand both, the tangential and axial stresses (σ_t and σ_a from equations (17) and (18)). With increasing fibre angle φ, the tensile strength of the CFRP wrapping in the tangential direction decreases, while the tensile strength in the axial direction increases.

$$\sigma(\varphi) = \frac{\sigma_{CFRP}}{SF} \cdot (1 - A \cdot \tan(\varphi)) \quad (19)$$

The wall thickness of the CFRP of the cylindrical section (T_{CFRP_0}) is increased in increments of 1mm and the procedure described above is repeated until the CFRP is able to withstand the tangential and axial stresses, respectively.

There are multiple approaches to determine the changing wall thickness for a dome wrapped with CFRP. Determining the thickness for a geodesic wound isotensoid dome is a commonly used approach and only requires knowledge about the wall thickness of the cylindrical section (T_{CFRP_0}) and the fibre angle (φ) [13]. Hence, this approach is used as a basis to determine the wall thickness of the CFRP wrapped over the dome-shaped lids ($T_{CFRP_{dome}}$). The resulting curve for the wall thickness of the dome ($T_{CFRP_{dome}}$) is shown in Figure 5.

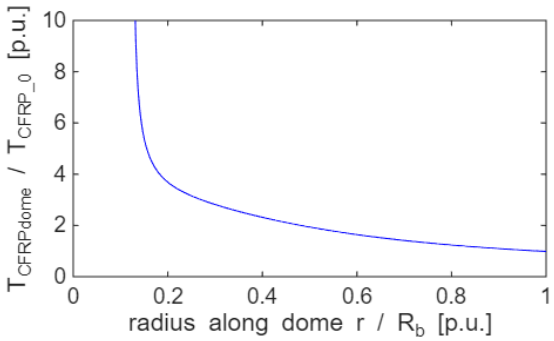

Figure 5: Thickness of a geodesic wrapped isotensoid dome along the radius of the dome. Both the X and Y axes are shown in per unit representation.

It is clear that the wall thickness ($T_{CFRP_{dome}}$) increases significantly near the axis of rotation (at r → 0) due to the overlapping of the fiber layers. Based on the curve for $T_{CFRP_{dome}}$ the outer contour of the dome-shaped lids wrapped in CFRP can be described using $z3(r)$, see equation (20).

$$z3(r) = \sqrt{(R_i + T_{PETG} + T_{CFRP_{dome}}(r))^2 - r^2} \quad (20)$$

The boss structures made from aluminum are not designed in detail. They are conservatively considered as solid blocks with a radius of $0.2 \cdot R_i$ and a height of $0.1 \cdot H_{total}$.

2.4 Inertia and mass calculation

At this point, all necessary wall thicknesses and fluid levels at the various operating points are known. The dome-shaped lids can also be clearly described mathematically applying the circle equations (3), (15) and (20).

For all components of the HVI-FW that can be described using simple geometric shapes, such as cylinders, cubes, spherical shells, etc., analytical solutions are used to calculate their moment of inertia [14].

For the remaining components that are described by the circle equations (3), (15) and (20), such as the dome-shaped lids made from CFRP, or the fluid in the hollow cylinder a numerical approach is used. These components are divided into a discrete number of hollow cylinder rings (indicated with the running variable i), with a wall thickness of dr, where $dr = R_i/1000$. The height h_i of such a hollow cylinder ring is then calculated, for example, from $h_i = z3(r_i)$ - $z2(r_i)$. With these parameters, the mass (m_i) and the inertia (J_i) can be calculated for each hollow cylinder ring according equations (21) and (22), respectively.

$$m_i = \rho \cdot \pi \cdot h_i \cdot ({r_{b_i}}^2 - {r_{a_i}}^2) \tag{21}$$

$$J_i = m_i \cdot \frac{{r_{a_i}}^2 + {r_{b_i}}^2}{2} \tag{22}$$

Where r_{b_i} and r_{a_i} are the outer and inner radii of each hollow cylinder ring.

To determine the total mass and the total inertia for each of those components, the sum of the segments indicated with i is calculated.

2.5 Energy calculation

In order to obtain the energy stored in the HVI-FW, its inertia is calculated for the nominal speed $J(n_0)$ and the lower speed limit $J(n_{low})$, respectively. Knowing the inertia at these speeds, equation (23) can be applied to derive the energy ΔE that can be released, when decelerating from n_0 to n_{low}. This calculation of energy represents a conservative approach, since $\Delta\omega$ and ΔJ are multiplied with the inertia at the lower speed limit (J_{low}) and angular velocity at the lower speed limit (ω_{low}). In reality, however, the change in angular velocity $(\Delta\omega)$ and the change in inertia (ΔJ) do not only occur at the lower speed limit, but continuously during deceleration from n_0 to n_{low}.

$$\Delta E = \omega_{low} \cdot (J_{low} \cdot \underbrace{\Delta\omega}_{\omega_0 - \omega_{low}} + \omega_{low} \cdot \underbrace{\Delta J}_{J(n_0) - J(n_{low})}) \tag{23}$$

3 Results and Conclusion

To find favourable dimensions of the HVI-FW for providing inertia (i.e. kinetic energy) to the electricity grid, the diameter of its inner and outer cylinders, as well as its height are varied, see Table 1. During a generation loss, the frequency can drop from 50 Hz to 47.5 Hz before an impermissible grid frequency is reached [8]. Hence, for each geometric configuration, the energy provided by the HVI-FW during a frequency drop from 50 Hz to 47.5 Hz is calculated. To find the optimal geometric configuration, and to reduce the material consumption compared to CFWs, the specific energy is derived. The design tool indicates that both the hollow cylinder radius (width) and the height of the HVI-FW should be as large as possible to maximize specific energy (see Figure 6). Because the same trend applies to CFWs, Figure 7 compares the specific energy of the optimal geometric configurations of the HVI-FW with that of CFWs. For

the CFWs, a CFRP rim with identical energy content, height, and outer diameter as the HVI-FW is considered. Figure 7 shows that the HVI-FWs achieve significantly higher specific energy, particularly at small radii. However, this advantage decreases continuously as the radius of the hollow cylinder increases and even reverses. Consequently, the design tool emphasises HVI-FW configurations with small hollow cylinder radii and thus relatively low power. This makes the HVI-FW a suitable choice for providing inertia to the electricity grid by coupling it to small synchronously rotating electrical machines, which are spatially well distributed and abundantly available. Therefore, the HVI-FW might be an effective solution for providing distributed and inherent inertia in future low-inertia power systems [15].

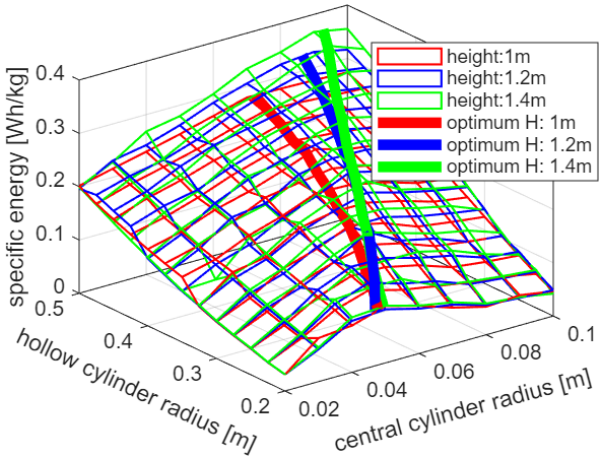

Figure 6: Specific energy of the HVI-FW in regard to its central cylinder radius, hollow cylinder radius and height (red for height = 1m, blue for height = 1.2m, green for height = 1.4m)

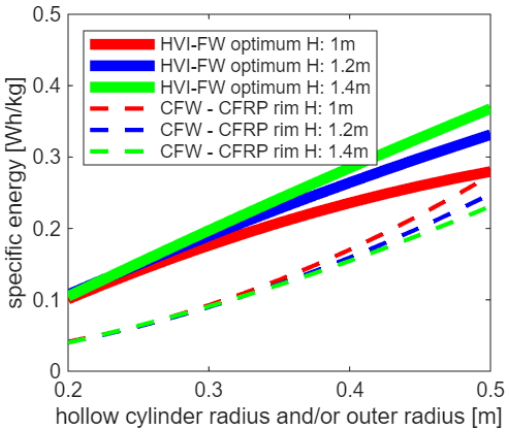

Figure 7: Specific energy for the optimal geometric configurations of the HVI-FW compared to the specific energy of CFWs

4 References

[1] H. Thiesen and C. Jauch, "Determining the Load Inertia Contribution from Different Power Consumer Groups," *Energies*, vol. 13, no. 7, p. 1588, 2020, doi: 10.3390/en13071588.

[2] A. Fernández-Guillamón, E. Gómez-Lázaro, and Á. Molina-García, "Extensive frequency response and inertia analysis under high renewable energy source integration scenarios: application to the European interconnected power system," *IET Renewable Power Gen*, vol. 14, no. 15, pp. 2885–2896, 2020, doi: 10.1049/iet-rpg.2020.0045.

[3] ENTSO-E. "Inertia and Rate of Change of Frequency (RoCoF): Version 17-SPD-Inertia TF." [Online]. Available: https://share.google/lsYyHNkl3A3wPelwy

[4] L. Mehigan, D. Al Kez, S. Collins, A. Foley, B. Ó'Gallachóir, and P. Deane, "Renewables in the European power system and the impact on system rotational inertia," *Energy*, vol. 203, p. 117776, 2020, doi: 10.1016/j.energy.2020.117776.

[5] Henning Thiesen, Arne Gloe, and Clemens Jauch, "Grid Frequency Data - WETI," 2022, doi: 10.17605/OSF.IO/JBK82.

[6] C. Jauch, R. Jost, and P. Kloft, "Hydraulic variable inertia flywheel," *Applied Energy*, vol. 360, p. 122830, 2024, doi: 10.1016/j.apenergy.2024.122830.

[7] A. Rettig, S. N. Jahromi, C. Jauch, and L. Reese, *Inherent Uninterruptible Power Supply via Directly Grid-Connected Machines and Variable Inertia Flywheels*, 2025.

[8] L. Reese, A. Rettig, C. Jauch, R. J. Domin, and T. Karshüning, "Joint Frequency Stabilisation in Future 100% Renewable Electric Power Systems," *Energies*, vol. 18, no. 2, p. 418, 2025, doi: 10.3390/en18020418.

[9] Wikipedia. "Shell integration." Accessed: Jan. 28, 2026. [Online]. Available: https://en.wikipedia.org/wiki/Shell_integration

[10] *AD 2000-Merkblatt: Zylinderschalen und äußerem Überdruck*, ICS 23.020.30, Verband der TÜV e.V., Jan. 2020.

[11] K.-H. Grote and J. Feldhusen, Eds. *Taschenbuch für den Maschinenbau,* 24th ed. Berlin, Heidelberg: Springer Vieweg, 2014.

[12] Daniel Heim. "Kohlenstofffaser verstärkter Kohlenstoff: Faser Matrix Anbindung und deren Einfluss auf den Kurzfaserverbund." Accessed: Jan. 28, 2026. [Online]. Available: https://mediatum.ub.tum.de/doc/1144388/document.pdf

[13] A. Air, E. Oromiehie, and B. G. Prusty, "Optimisation of a composite pressure vessel dome using non-geodesic tow paths and automated fibre placement manufacturing," *Composites Part B: Engineering*, vol. 288, p. 111906, 2025, doi: 10.1016/j.compositesb.2024.111906.

[14] Wikipedia. "List of moments of inertia." Accessed: Jan. 28, 2026. [Online]. Available: https://en.wikipedia.org/wiki/List_of_moments_of_inertia

[15] L. Reese, A. Rettig, and C. Jauch, "Future Frequency Stabilisation By Innovative Hydraulic Variable Inertia Flywheel," submitted for publication at conference 19. SYPOSIUM ENERGIEINNOVATION (2026).